

Chapter 5

Crystallization of Cpx in the Ab-Di System Under the Oscillating Temperature: Contrast Dynamic Modes at Different Periods of Oscillation



Alexander G. Simakin, Vera N. Devyatova, and Alexey N. Nekrasov

Abstract The evolution of the texture of a partially crystallized melt at a temperature oscillating around liquidus has been experimentally investigated. The model pseudobinary albite—diopside system was used, in which the clino-pyroxene is the only phase formed under the experimental conditions $P = 200$ MPa, $T = 1050$ – 1150 °C, $C_{H_2O} = 3.3$ wt%. All products of the experiments were characterized by the Crystal Size Distributions (CSD) measured by BSE image analysis. Due to the high nucleation rate of clinopyroxene and the slow cooling rate of about 100 °C/min a large volume of quenching crystals was formed with residual glass approaching pure albite in composition. The quench tails were identified, and parts of the CSD formed prior to quenching were restored. In the CSD recovery procedure, we used an estimate of the equilibrium volume of Cpx, based on an experimentally verified melting diagram. We also assume that the crystal growth rate at quenching can be approximated as a size-independent parameter. In the experiment yielding the largest crystals, the Cpx cores formed prior to quenching were identified using microprobe observations, and their sizes were estimated from BSE images. The measured size distribution of the cores of Cpx crystals turned out to be close to the restored CSD. In our experiments, the variable period of temperature oscillations in the same range of $1135 < T < 1155$ °C was a parameter controlling the texture. With a large period of oscillation (about an hour), all crystals dissolve at the hot stage and reprecipitate in a cold one, which leads to the formation of log-linear CSDs. The shortest oscillation period of 4–10 min results in a gradual maturation of the texture with time with a decrease in the number density of crystals, and CSD evolved to a log-normal shape with a maximum. The growth rate independent of the crystal size is essential for effective ripening with temperature oscillations. Simple calculations show that with diffusion control of both dissolution and growth, only the first temperature oscillation affects CSD.

A. G. Simakin (✉) · V. N. Devyatova · A. N. Nekrasov

D.S. Korzhinskii Institute of Experimental Mineralogy, Russian Academy of Science, Osipyana 4, Chernogolovka, Moscow Region 142432, Russia

e-mail: simakin@ifz.ru

A. G. Simakin

O.Yu. Schmidt Institute of Physics of the Earth, Russian Academy of Science, Bolshaya Gruzinskaya, 10-1, Moscow 123242, Russia

© The Editor(s) (if applicable) and The Author(s), under exclusive license to Springer Nature Switzerland AG 2020

Y. Litvin and O. Safonov (eds.), *Advances in Experimental and Genetic Mineralogy*, Springer Mineralogy, https://doi.org/10.1007/978-3-030-42859-4_5

Keywords Melt · Crystal growth · Nucleation · CSD

5.1 Introduction

Shortly after the birth of a new Academic cluster (settlement, village) in Chernogolovka in 1969 a small research center for Earth Science was created, called the Institute of Experimental Mineralogy. Mark Epelbaum was close to the founding fathers of IEM and from the very beginning he headed igneous studies, aimed at the investigation of silicate melts and especially their dynamic properties, such as diffusion (Chekhmir et al. 1991), viscosity (Epel'baum 1980) and crystallization kinetics. As a man who began his career in the field of industrial glass and ceramics, M. B. Epel'baum realized the importance of understanding how crystalline phases nucleate and grow from a melt for the manufacture of glass and silicate materials. Over the next decades, magmatism lab researchers learned how the dynamics and kinetics of crystallization can affect natural processes: in volcanoes, small sills and dykes and large intrusions. Important results were obtained on the experimental measurement of the growth rates of magmatic minerals: feldspar from granite (Simakin and Chevychelov 1995), plagioclase (Simakin and Salova 2004), and clinopyroxene (Simakin et al. 2003) from hawaiitic melts. Experimental studies of magma crystallization caused by degassing were initiated by our early work with the Pietro Armienti (Simakin et al. 1999). The first results of numerical simulation of the growth and deposition of crystals in the kinetic approach using the CSD functions were obtained in Simakin et al. (1998).

In episodes of fast solidification caused by decompression and degassing, convective mixing of magmas contrasting in composition or temperature, flushing of hydrous magmas with carbonic fluid—deviations from equilibrium of the melt and magmatic minerals are high on a large scale and the kinetics of nucleation and growth becomes important. Spatially homogeneous sets of nucleating and growing crystals can be described with crystal size distribution (CSD) functions. Existing models (e.g., Brandeis et al. 1984; Toramaru 1991; Hort 1998), which neglect the effect of crystal settling are actually extended forms of the Avrami-Kolmogorov equation (Avrami 1939) and do not require the explicit use of CSD. The crystal size distribution becomes especially important for modeling the crystal settling in solidifying intrusions with a Stokes rate proportional to the square of the crystal radius. When solidification with crystal settling is simulated (Simakin et al. 1998), CSD gives an extra dimension (crystal size) and the problem generally turns from 3D into 4D ($F(t, x, y, z, R)$).

There have been attempts to measure and use CSD of magmatic minerals as such in petrological practice. Decades ago Marsh (1988) proposed a model that pretended to extract some useful information from the parameters of log-linear CSDs typical for quickly solidified magmatic rock. In this model it is assumed that magma enters the chamber, crystallizes, being perfectly mixed, and is permanently evacuated with periodic eruptions. Then, at constant growth and nucleation rate, parameters of CSD

are related to the average residence time of the magma in a chamber. This model had been arbitrarily applied to a closed system, such as the lava lake (Cashman and Marsh 1988). The inadequacy of the model became apparent when Vona et al. (2011), Vona and Romano (2013) tried to use it to interpret experimental data on the dynamic melt crystallization in a rotational viscometer. There were two generations of crystals in their experiments: one formed in the main stage of experiment and second at quenching. In the first publication (Vona et al. 2011) the authors considered only those parts of CSDs that were formed during quenching, since they had log-linear form and could be interpreted in a conventional manner (Marsh 1988). In the second paper, based on these data, Vona and Romano (2013) dropped the quenching parts and get reasonable estimates of growth rates from the rest of the CSDs based on the results of viscosity measurement.

About decade ago, Simakin and Bindeman (2008) theoretically investigated effect of a series of dissolution and precipitation events in the system crystals-melt. Formation of logarithmic normal like shape of CSD typical for zircon and quartz phenocrysts in some large volume rhyolites was explained. Assumed periodic rapid heating and gradual slow cooling is a common mode for the long-lived magma chambers under volcanoes. The parameters of CSD can be semi-quantitatively interpreted with this model to estimate the number and strength of such events. Several experimental studies have focused on the evolution of CSD with periodic oscillations in temperature (Cabane et al. 2005; Mills and Glazner 2013). An experimental study conducted by Mills and Glazner (2013) did find ripening of CSD of olivine in a basalt melt with the applied temperature oscillations with a decrease in the volume number content of crystals.

Later, model of Simakin and Bindeman (2008) was questioned in Bindeman and Melnik (2016) based on the results of the simplified numerical simulation of the dissolution and growth of zircon crystals. The main difference in the models used in (Simakin and Bindeman 2008; Bindeman and Melnik 2016) is representation of the crystal growth rate as size independent or diffusion controlled (inversely proportional to size) processes, respectively. Direct observations of the crystallization of olivine from basalt melt in a moissanite cell lead Ni et al. (2014) to conclude that the rate is proportional to size, which is opposite to the dependence expected in diffusion control. Due to the complexity of this problem, experimental observations can make a valuable contribution to its solution.

This paper presents the results of an experimental study of clinopyroxene crystallization from the model Ab-Di melt with temperature oscillations. In experiments conducted by Mills and Glazner (2013), the temperature always oscillated below the liquidus of the phases under consideration. In our experiments, we applied oscillations with a different period when the temperature rises above the liquidus as in the periodically replenished magma chambers. We have shown that diffusional dissolution time of the largest crystals t_{dissol} becomes a parameter controlling the contrasting dynamic modes of textural evolution. We precisely measured CSD of clinopyroxene and show that the approximation of the size independent growth is applicable. Theoretically, we also demonstrated that, size-independent crystal growth rate leads to the maturation of the CSD with experimentally observed rates.

5.2 Experimental Method

Experimental strategy. For our research, we chose a simple pseudo-binary Ab-Di system. At $P_{\text{H}_2\text{O}} = 2$ kbar it is characterized by a melting diagram with an essentially single diopside + melt (Di + L) field (Yoder 1966; Pati et al. 2000). It is pseudo-binary because of the presence of Ca in plagioclase and enstatite in diopside. The plagioclase + clinopyroxene + melt field exists near the solidus temperature $T_s = 820\text{--}830$ °C and a tiny phase field of plagioclase in equilibrium with melt occurs near the albite edge (see Fig. 5.1). Such an elementary diagram simplifies interpretation of the experimental data and the CSD measurements. When the fluid pressure rises from $P_{\text{H}_2\text{O}} = 1$ ($C_{\text{H}_2\text{O}} \approx 4$ wt%) to 2 Kbar ($C_{\text{H}_2\text{O}} \approx 5.6$ wt%), T_1 decreases insignificantly as reflected in the position of the Cpx liquidus for $P_{\text{H}_2\text{O}} = 1$ Kbar approximately plotted in Fig. 5.1 as a line connecting corresponding diopside and albite melting points. This is explained by the fact that the first percentages of water dissolved mainly as hydroxyl formed by a reaction with an aluminosilicate melt, thereby greatly reducing the temperature of the liquidus (T_1) of the diopside. With a larger content, the water dissolves mainly in molecular form and has a smaller effect on the melting

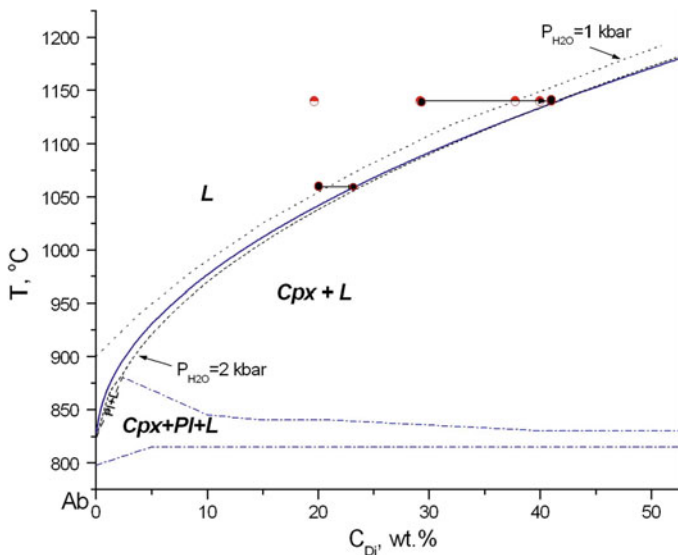


Fig. 5.1 The pseudo-binary melting diagram of Ab-Di system; the liquidus curve of Cpx at $P_{\text{H}_2\text{O}} = 2$ Kbar (Yoder 1966) is shown by a short-dashed line, liquidus at $P_{\text{H}_2\text{O}} = 1$ Kbar is approximately plotted on the basis of the melting temperatures of diopside and albite, since there are no direct experimental data. For $P_{\text{H}_2\text{O}} = 2$ Kbar additional fields Pl + L and Cpx + Pl + L are shown. The points on the plot depict our results with the starting compositions in the Ab-Di system with an excess of silica (see text) and $C_{\text{H}_2\text{O}} = 3.3$ wt%; semi-filled circles correspond to a pure melt, pair of small filled circles (some superimposed) display experiments with seeds, reflecting the original and diopside saturated compositions linked by an arrow. Our approximation of the Cpx liquidus is shown by a solid line

Table 5.1 Composition of the starting materials

	SiO ₂	Al ₂ O ₃	MgO	CaO	Na ₂ O	K ₂ O
Ab ₈₀ Di ₂₀ (13) ^a	67.03 (0.34) ^b	15.50 (0.22)	3.99 (0.17)	4.35 (0.15)	8.90 (0.26)	0.22 (0.05)
Ab ₇₁ Di ₂₉ (8)	66.09 (0.56)	14.15 (0.23)	5.64 (0.30)	5.94 (0.07)	7.9 (0.36)	0.14 (0.04)
Ab ₅₅ Di ₄₅ (8)	65.54 (0.28)	10.49 (0.32)	9.27 (0.12)	8.50 (0.21)	6.06 (0.12)	0.14 (0.06)
diopside (seed. 11)	56.36 (0.33)	0.21 (0.05)	17.71 (0.11)	26.28 (0.11)	0.12 (0.07)	0.09 (0.04)

Electron microprobe analyses of glasses are normalized to 100%

^a number of analyses, ^b one standard deviation

diagram. Thus chosen composition demonstrated low sensibility to the local water concentration variations caused by the probable inhomogeneity of the starting glass and induced by crystallization.

The experimental apparatus The experiments were performed in an internally heated pressure vessel (IHPV) with free volume 262 cm³ made of a stainless steel, held vertically. Temperatures during the experiment were measured by an external unshielded Pt-Rh thermocouple, thermal gradient free zone is 40–50 mm. The thermocouples were calibrated against the melting of Au at 1000 bar. Pressure was measured with transducers with accuracy of 5%. The temperature was maintained with a precision of ± 2.5 °C and recorded digitally. At the end of experiments the furnace was turned off and the temperature was lowered to T = 600 °C level for a few minutes at the cooling rate about 150°/min along with the vessel cooled with running water.

Starting materials. We prepared the starting mixtures using synthetic gels of albite and diopside compositions (see Table 5.1). Mixtures of powdered and carefully mixed components were loaded into a Pt capsule. Glasses with different albite contents were prepared by heating to 1450 °C in a high-temperature furnace at an ambient pressure for 5 h. Dry glasses were studied using SIM-EDS and X-ray methods. The synthesized glasses (see Table 5.1) contained a small amount (5–6 wt%) of excess SiO₂ in comparison of the target glasses of Ab-Di composition and were practically crystal free. During the next step, hydrous glasses were prepared in an IHPV at P = 1 kbar and T = 1250 °C during 24 h. In this synthesis large Pt capsule was loaded with 1 g of the dry glass and 45 mg of water. The water content in the homogeneous glasses without bubbles was determined by KFT method. Water content demonstrated systematic increase with rising albite content and comprises: Ab₅₅—3.33 wt% Ab₆₀—3.35% Ab₇₀—3.42 wt%, Ab₈₀—3.69 wt%. The later value approaches water solubility in the albite melt of about 4 wt% at P = 1 kbar and T = 1250 °C (McMillan and Holloway 1987). At P = 2 kbar the residual melt becomes water—saturated only when practically all Cpx crystallizes upon quenching as follows from the mass balance calculation that excludes vesiculation. All dynamic crystallization experiments were conducted with the starting glass Ab₅₅. Glasses with

other compositions were used in the preliminary experiments on the Cpx liquidus determination.

Experimental regimes. Pt capsules with diameter 3 mm were loaded hydrous glass powder, welded and placed in the temperature gradient free zone of the IHPV furnace. In experiments the temperature oscillated with different periods from $T = 1155\text{ }^{\circ}\text{C}$ slightly above to $T = 1135\text{ }^{\circ}\text{C}$ moderately below the liquidus (see Table 5.2). The diopside crystals (Ioko-Dovyren intrusion skarns, North Transbaikal Territory) were used in some preliminary runs aimed on the Cpx liquidus determination.

5.3 Analytical Methods

Phase compositions of the each run products were studied. Samples were prepared by mounting the products of the runs in polystyrene and polishing one face of a polystyrene cylinder. The textural and chemical analyses were performed using a CamScan MV2300 and Tescan Vega TS5130MM SEMs with an energy-dispersive spectrometer (INCA Energy 450) at the Institute of Experimental Mineralogy, Chernogolovka, Moscow region, Russia. The spectrometer was equipped with semi-conductive Si(Li) detector INCA PentaFET X3. All the phases were analyzed at an accelerating voltage of 20 kV, the current of the absorbed electrons on the Co sample was 0.1–0.2 nA. The smallest beam diameter was 0.2 μm for point phase analysis, the glasses were analyzed using a rectangle scanning area with a width of up to 50–80 μm . The measurements results were processed by the software package INCA Energy 200. Qualitative X-ray analysis of the run products was performed on a Bruker “D2 Phaser” desktop diffractometer with a copper anode for X-ray powder diffraction.

The water content was determined with the Karl Fischer titration (KFT) method on a KFT Aqua 40.00 with a HT 1300 high-temperature solids module. Detectable water weight (m_w) range: 1–100 mg, reproducibility: $\pm 3\text{ }\mu\text{g}$ at m_w 1–1000 μg , 3% at the $m_w > 1\text{ mg}$. With a common glass sample weight 20 mg and water content in the range 1–3 wt% precision is more than 1.5% relative.

5.4 CSD Measurements

We studied the CSD by analyzing backscattered electron images (BSE) of the surfaces of our samples. First, the images were analyzed using *ImageJ* 1.48v. Then the CSDs were calculated using the *CSD-Corrections* 1.40 software (Higgins 2000, 2002). In the chosen system the number density of crystals was high, and the typical value of counts for each measured sample ranged from 1200 to 2000, with the exception of 428 counts for the 72 experimental run, which involved the largest crystals (see Table 5.3). The shape of the crystals for each experiment was estimated by fitting the observed distribution of the width/length (W/L) ratio of crystals cross-sections

Table 5.2 Conditions of the experiments and observed phases

Run #	Initial comp.	Seed	Number of cycles	T ₁ (°C)	t ₁ (min)	T ₂ (°C)	t ₂ (min)	Products
<i>Liquidus estimation</i>								
10	Ab ₅₅ Di ₄₄	—	0	1250	1440	1140	1440	Glass
13	Ab ₈₀ Di ₂₀	—	0	1250	1440	1140	1440	Glass
18	Ab ₅₅ Di ₄₄	+	0	1250	30	1140	1440	Glass + Cpx
14	Ab ₅₅ Di ₄₄	+	0	1250	30	1100	1440	Glass + Cpx
16	Ab ₈₀ Di ₂₀	+	0	1250	30	1100	1440	Glass
21	Ab ₇₄ Di ₂₆	+	0	1250	30	1060	240	Glass + Cpx
27	Ab ₈₀ Di ₂₀	+	0	1250	20	1040	240	Glass + Cpx
28	Ab ₅₅ Di ₄₄	+	0	1250	20	1040	240	Glass + Cpx
<i>Crystallization at the oscillating temperature</i>								
72	Ab ₅₅ Di ₄₄		3	1155	60	1135	60	Glass + Cpx
60	Ab ₅₅ Di ₄₄		2	1155	45	1135	45	Glass + Cpx
54	Ab ₅₅ Di ₄₄		4	1155	45	1135	45	Glass + Cpx
61	Ab ₅₅ Di ₄₄		8	1155	20	1135	20	Glass + Cpx
56	Ab ₅₅ Di ₄₄		5	1155	20	1135	20	Glass + Cpx
86	Ab ₅₅ Di ₄₄		3	1155	20	1135	20	Glass + Cpx
49	Ab ₅₅ Di ₄₄		5	1155	5	1135	5	Glass + Cpx
48	Ab ₅₅ Di ₄₄		1	1155	5	1135	5	Glass + Cpx
50	Ab ₅₅ Di ₄₄		5	1155	2	1135	2	Glass + Cpx
52	Ab ₅₅ Di ₄₄		1	1155	120	1135	120	Glass + Cpx
51	Ab ₅₅ Di ₄₄		2	1155	90	1135	90	Glass

Table 5.3 Results of CSD measurements

Run #	Number of measured crystals	Relative area ε_s	Crystals habitus: ellipsoid axes ratios	Maximum length	Correction factor γ	N_{eq} (μm^{-3})	Mean dist. between crystals (μm)
72	428	0.350	1/1.3/1.6	38.8	1.09	0.14e-03	19
	70	0.034	1/1.25/1.6	15.8	–	–	–
60	1316	0.30	1/1.9/2	31.1	1.31	0.49e-03	12.7
54	1543	0.32	1/1.25/1.3	15.2	1.15	2.04e-03	7.9
61	1539	0.277	1/1.9/1.9	23.8	1.33	1.36e-03	11.3
56	1408	0.301	1/1/2.2	15.3	1.44	6.43e-03	5.4
86	1200	0.310	1/1.2/3	15.6	1.32	38.72e-03	2.9
49	1939	0.318	1.0/1.3/2.7	15.6	1.15	10.6e-03	4.6
48	1020	0.305	1/1.2/3	17.6	1.41	8.72e-03	4.8
50	1905	0.268	1/1.50/5.00	13.8	1.36	24.7e-03	3.7

to the model distribution with the *CSD-Corrections* software. The shape was chosen using manual visual selection of the minimum misfit following instructions for the program. For run 56 more detailed work was performed. Based on these calculations the uncertainty of the shape factors is approximately 10–13% (1σ). To further use all the measured CSDs, the $\lg(n(L))$ was approximated using polynomials on L of an order up to 4. Some distributions with a second part at small sizes were approximated using piece-wise continuous functions.

In the program *CSD-Corrections* we used a roundness parameter value of 0.5–0.7 as a value obtained by the averaging by the individual crystals from *ImageJ*. Therefore, on average, the volume fraction calculated for the ellipsoids while using our polynomial representations of density function ($\varepsilon_{s,cSD}$) was underestimated in comparison to the observed value (ε_s) of $(\varepsilon_{s,cSD} - \varepsilon_s)/\varepsilon_s = -0.32 \pm 0.17$. Theoretically, this parameter should have a value of $\Delta\varepsilon_s/\varepsilon_s = -(0.31-0.39)$ because *CSD-Corrections* distribution was scaled for crystals with a shape factor intermediate between block and ellipsoid in accordance with roundness parameter. Small deviations of $\Delta\varepsilon_s/\varepsilon_s$ from theoretical value can be explained by different representations of $n(L)$ at integration and the merging effects of different measurements sets (images) for a particular run. A scaling parameter γ was applied to each approximation of distributions to satisfy the equality of the volume fraction of the crystals and the measured relative cross-sectional area of the crystals (ε_{2D}) as follows

$$\gamma = \varepsilon_{2D} / \int_0^{L_{\max}} n(l)V(l)dl, \quad V(L = L_3) = \frac{4}{3}\pi L_1 L_2 L_3$$

$$= \frac{4}{3}\pi L_3 \frac{L_1}{L_3} L_3 \frac{L_2}{L_3} L_3 = \alpha L^3 \quad (1)$$

where α is a shape factor equal to $\alpha = \frac{\pi L_1 L_2}{6L_3^2}$, and the axes of the approximating ellipsoid are ranked as follows $L_1 \leq L_2 \leq L_3$.

5.5 Experimental Results

5.5.1 Melting Diagram

We check the position of the pyroxene liquidus at $P_{\text{total}} = 2$ kbar and $C_{\text{H}_2\text{O}} = 3.3$ wt%. Compositions Ab₈₀, Ab₇₀, Ab₆₀ were held at $T = 1140$ °C for 5 h and pure quenching glasses were obtained (see Fig. 5.1) arguing for their location in the liquid field of the melting diagram. At $T = 1060$ °C, the Ab₈₀ composition was also quenched in the pure glass. Position of the Cpx liquidus was further ascertained with probing crystal technique. Would diopside crystal be placed in the Cpx undersaturated melt it dissolves with concentration on the boundary becoming close to the Cpx liquidus in Ab-Di system. At the start of crystal probing experiment we preheat Ab₈₀ + Di and Ab₇₀ + Di assemblages at 1250 °C for 30 min and then held at temperature of experiment $T = 1050$ and $T = 1150$ °C respectively for 48 h. During the preheating stage, crystals were partially dissolved, and a wide diffusion zone was formed. Upon cooling to the temperature of the experiment, an excess of diopside in the diffusion zone precipitated. Thus in the main stage of experiment diffusion between two-phase zone and pure melt had place. Concentration of Di on the boundary between two-phase zone and pure melt corresponds to the Di liquidus. The products of the quenching of the pure melt and the two-phase zone differed significantly which makes it possible to evaluate the equilibrium composition at their boundary. To estimate the composition of the pre-quenching melt, a sufficiently large rectangular area of crystals and quench glass up to 50×5 μm was used during the EDS. Two starting and equilibrium compositions were connected as shown Fig. 5.1 by the arrows. In the range of the compositions under study, we found a good agreement with the data published for the Ab-Di system at $P_{\text{H}_2\text{O}} = 2$ kbar (see Fig. 5.1). The effect of excess 5–6 wt% of SiO₂ in the Ab-Di melt compensates effect of the water concentration of 3.3 wt% lower than $C_{\text{H}_2\text{O}} \approx 5.5$ wt% in the melt saturated at $P_{\text{H}_2\text{O}} = 2$ kbar.

5.6 Crystallization Experiments

5.6.1 Sample Textures

For the selected composition of the Ab₅₅Di₄₅, the liquidus temperature is $T_l = 1150$ °C. The temperature oscillations have a rectangular shape: during the first half-cycle, the temperature was set at $T = 1155$ °C or 5 °C above the liquidus, and during the second half-period it was reduced by 15 °C below the liquidus at $T = 1135$ °C.

A wide variety of runs regimes led to a great variety of relatively spatially uniform textures, specified by the size and habitus of Cpx crystals. The maximal size of Cpx varied from c.a. 10–50 μm . The volume fraction of Cpx approached the full precipitation limit, which was estimated as 0.355 for the $\text{Ab}_{55}\text{Di}_{45}$ composition. The equilibrium volume fraction of Cpx reached during the main stage of experiment was much smaller. For the melt $\text{Ab}_{55}\text{Di}_{45}$ it was 0.046 for undercooling ΔT of 15 $^{\circ}\text{C}$. This meant that the main volume of Cpx is precipitated during the quenching stage. Volume fraction of the equilibrium part of crystals is about 0.14, which translates into an equilibrium radius of approximately half of the total.

The habit of the crystals varies from more or less isometric (the ranked ratio of the axes of the approximating ellipsoid is 1/1.2/1.3 ($L_1/L_2/L_3$) for run 54) to a highly elongated (1/1.3/5 for run 68). To correctly compare the distributions of crystals with the different shapes, we mutually plot these dependences using the corrected (equivalent) size parameter $L^* = L\sqrt[3]{(L_1/L_3)(L_2/L_3)}$, where the largest crystal size is L_3 . This relation can be reformulated as $L^* = \sqrt[3]{L_1 L_2 L_3} \propto \sqrt[3]{\text{volume}}$.

During all experiments with melt, the final stage is quenching with different technically available rates. The crystals continue to nucleate and grow during quenching, thus modifying the CSD formed during the main stage of the experiment. The quenching effect can be eliminated, and the original CSD can be reconstructed. In this study, we assumed that CSD shape does not deform during growth, and only shifts to the larger sizes. This is true when the growth rate is crystal-size independent and the melt composition is homogeneous. In this case, it is clear how to restore CSD for the main stage of the experiment, removing the quenching effect. We calculated dL (L —is the largest crystal dimension), so that the volume fraction of the crystals for the measured density with the argument $n(l + dL)$ ($l + dL \leq L_{\text{max}}$) becomes equal to the equilibrium value as follows:

$$\int_0^{L_{\text{max}}-dL} \gamma a \cdot n(l + dL) \cdot (l/2)^3 dl = \varepsilon_{eq}, \quad (2)$$

where ε_{eq} the equilibrium crystal volume fraction. This linear transformation implies that the smallest crystals ($l = 0$) at the end of the main stage of the experiment obtain the size dL after quenching. The value of dL splits the density function into parts related to the main and quenching stages of growth. The partition of acquired CSDs is shown in Figs. 5.2, 5.3 and 5.4.

After separation of the equilibrium part of the CSD, we calculated the number density of Cpx crystals N_{eq} with the eliminated quenching effect as follows:

$$N_{eq} = \int_0^{L_{\text{max}}-dL} \gamma \cdot n(l + dL) dl \quad (3)$$

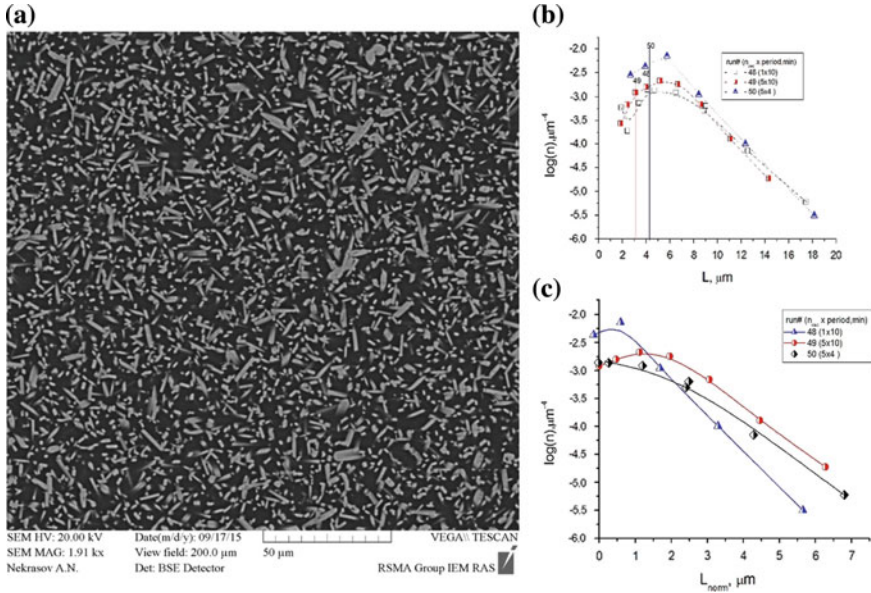


Fig. 5.2 Experiments in which the half-period of the temperature oscillations is less than the dissolution time of Cpx crystals. **a** BSE image of sample from run 50—5 oscillations with period 4 min; the texture demonstrates very weak ripening. **b** Full CSDs, vertical lines divide plots on the quenching and main parts. **c** The restored CSDs formed before quenching, densities plotted versus effective (proportional to crystal volume in order 1/3) maximum crystal dimension. The CSD of the Cpx crystals from run 49 is the most matured in this series

The values of the calculated N_{eq} are shown in Table 5.3. It can be seen that the restored crystal density changes by three orders of magnitude, depending on the experimental conditions. Based on the measured CSDs, we calculated the average crystal size as the first moment of distribution and the mean inter-crystalline distance as $l \approx 2/(N_{eq})^{0.333}$; the values of these parameters are also listed in Table 5.3. The inter-crystalline distance characterizes the diffusion ability to provide a low supersaturation in the melt volume at rapid cooling. When this distance was sufficiently large, the flat crystal faces became morphologically unstable during quenching and the hopper overgrowth is formed.

5.7 Products Composition

The EMPA analyses demonstrated (see Table 5.4) that the experimentally grown diopside was a solid solution containing up to 7 wt% of enstatite. This content is near to the solvus composition of Cpx ($\text{Di}_{90}\text{En}_{10}$) in the En-Di system at $T = 1000^\circ\text{C}$ (Boyd and Schairer 1964). The alumina content in Cpx is in the range 0.3–2 wt%. To characterize the composition of the residual glass, we used SEM-EDS analysis

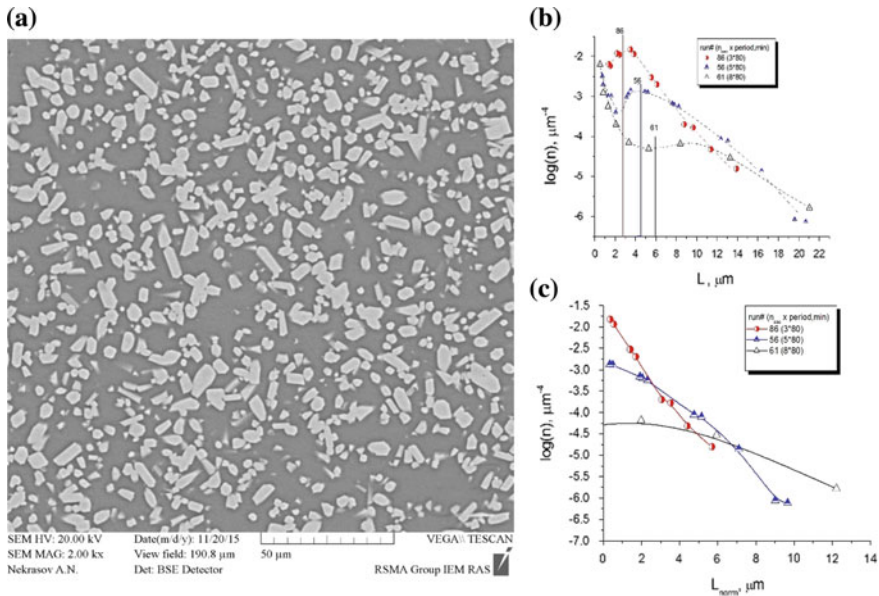


Fig. 5.3 Experiments in which the half-period of the temperature oscillations is near the dissolution time of the Cpx crystals, additional crystals nucleated in the cold half-cycle. The original log-linear CSD evolves towards the right-skewed form with a maximum. **a** BSE image of sample from run 56—5 oscillations with period of 80 min. **b** Full CSDs, vertical lines indicate dL and divide plots on the quenching and main parts, for run 56, the interval (level 1σ) for dL is outlined by a rectangle. **c** The restored CSDs formed before quenching

averaged over the surface of polygons selected between crystals with an area of approximately $20\text{--}100\ \mu\text{m}^2$. The glasses were enriched in Na and Al and depleted in Mg and Ca in comparison to the starting composition. The proportions of the increments in the concentration of elements can approximately be described as the diffusive mixing of albite and diopside in a melt instead of individual oxides. During experiments with a higher number density of crystals (48, 49, 50), the averaged melt composition was more enriched in albite. For these runs, the volume fraction of Cpx calculated on the basis of the glass composition was only slightly less than the volume fraction observed in the BSE images (relative difference 2–5%). For the other experiments, the residual glass contained less albite, and the difference between the measured and calculated solid fraction was greater (up to 29% in run 72). From this comparison, it follows that during the last stage (at a temperature approaching T_g) of quenching, the residual melt composition of the later runs, on the average, was not on pace with the albite flux from the growing Cpx crystals when forming sharp diffusive boundary layers. This effect is the most pronounced at the longest inter-crystalline distance corresponding to the smallest number density of the crystals during the run 72 that had unstable rims with hopper morphology.

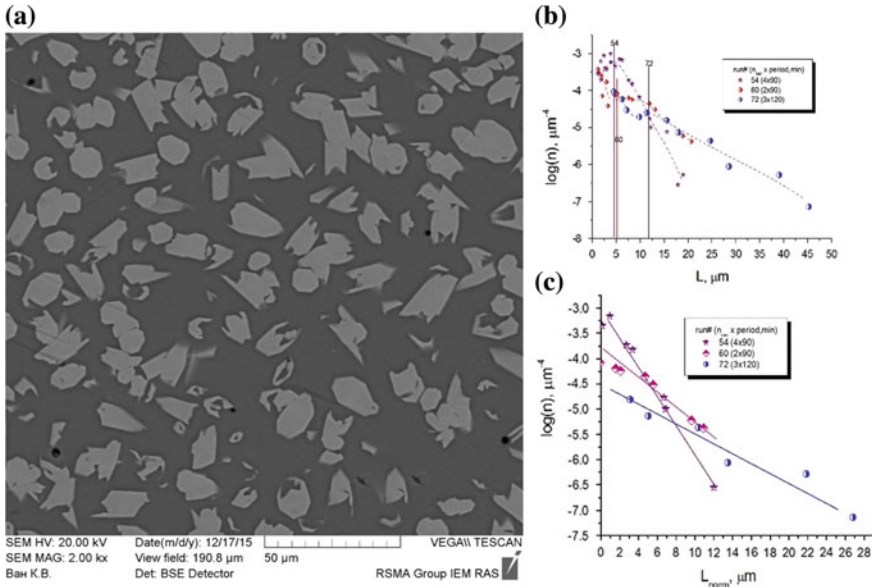


Fig. 5.4 The CSDs of Cpx in experiments in which the half-period is longer than the dissolution time. All the crystals were completely dissolved in the hot half-cycles and nucleated in the cold ones. **a** BSE image of sample from run 60—2 oscillations with period 1 h 30 min. **b** Full CSDs, vertical lines indicate dL and divide plots on the quenching and main parts. **c** The restored CSDs formed before quenching are near the log-linear in shape

5.8 Effect of the Variable Period of the Oscillations

In experiments with an oscillating temperature during the cold half-cycle, the nucleation and crystal growth of Cpx occurred at a moderate undercooling of a $\Delta T = 15\text{ }^\circ\text{C}$, and during the hot half-cycle crystal dissolution occurred at a temperature exceeding the liquidus at $5\text{ }^\circ\text{C}$. Superheating above the liquidus means that for a sufficiently large oscillation period, all the crystals dissolve. The time required for the dissolution of crystals of different sizes was estimated on the basis of experimental data on diffusion in the magma and will be discussed below. According to the oscillation period experiments can be divided into four groups.

- (1) At the largest thermal oscillations period of three hours all crystals dissolved in the hot stage. At the same time, the concentration of clusters with large dimensions, but less critical for nucleation at the cold stage, decreased. With such a long superheating treatment, during run 51 after the second cold half-cycle, pure quenching glass with a few dendrites heterogeneously nucleated from the capsule wall was formed. This was possible only if the delay time of the nucleation after the hot half-cycle was longer than 1.5 h.
- (2) During experiments with the shortest period of 4–10 min (runs 48–49–50), the crystals dissolved only slightly. Cpx crystals in these runs showed the largest

- elongation (for the run 50 shape coefficients are 1/1.5/5, see Fig. 5.2a). In this group, the density functions, restored for the equilibrium stage, increased in maturation in the sequence of runs 50–48–49 (see Fig. 5.2b, c). With an increase in the degree of ripening an explicit maximum appears in the series of the dissolution-precipitation events and shifts to larger dimensions, as the model predicted (Simakin and Bindeman 2008). The maximum is recognized better on the initial plot not subjected to the quenching effect elimination (Fig. 5.2b). Because of intrinsically stochastic nature of the nucleation process, the initial stage of experiments 48, 49 and 50 with respect to N_{eq} can differ in order of magnitude there is no single dependence $N_{eq}(t)$.
- (3) In the third group of experiments with a period of 40 min (runs 86, 56, 61), the crystals dissolved significantly during the hot half-cycle; therefore, new crystals nucleated during the cold half-cycle. The crystals in this group have more isometric than in the previous group habitus (Fig. 5.3a, Table 5.3). Relatively large number density and small inter-crystalline distance provide low supersaturation and smooth overgrowth at quenching. The restored CSDs after 3 and 5 oscillations had a log-linear form (Fig. 5.3b, c). The average size increased and the number density of the crystals appreciably decreased. After 8 oscillations, the CSD reached a weakly expressed maximum which is better seen in the initial CSD (Fig. 5.3b).
 - (4) Finally, in the fourth group of experiments, the period of oscillation was 90–120 min. Maturation in this set is prominent, and the largest (up to 45 μ) nearly isometric crystals were formed (Fig. 5.4a). Two and five oscillations with a period of 90 min (runs 60 and 54) provided the CSDs with a shape that was near log-linear (Fig. 5.4b, c), as in the experiment 72 (3 oscillations with a period of 120 min). At quenching the crystals were overgrown with morphologically unstable (hopper-like) rim due to low crystal number density and large inter-crystalline distance (Table 5.3). We assumed that all the crystals dissolve during the hot stage and nucleated back during the cold stage. It is noteworthy that N_{eq} for run 60 (2 cycles) is less than that for run 54 (4 cycles) (see Table 5.3). Such irregularity may reflect complete dissolution and homogeneous nucleation with each oscillation with a stochastic result. Composition of the sufficiently large Cpx crystals with the largest dimension up to 45 μ m from run 72 (Fig. 5.5a) was studied with the EDS.

The core region with an increased Al_2O_3 content was surrounded by an inner rim with a low Al_2O_3 content; the outer quenching rims are returned back to a higher Al_2O_3 content (see Fig. 5.5b). A minimal Al_2O_3 content of 0.35 wt% was observed in the inner rim surrounding the core. For the series of measurements ($n = 12$), the minimal concentration of aluminum oxide was 0.34 ± 0.12 wt%. The distribution of MgO (and opposite CaO) in these crystals also demonstrated a clear compositional zoning (see Fig. 5.5c): the core with a high CaO content is surrounded by an inner rim with the highest MgO content, and the outer quenching rims return back to a higher CaO content. Correlation coefficient of Ca and Mg concentrations in the Cpx from run 72 is -0.89 in accordance with Di-En mixing.

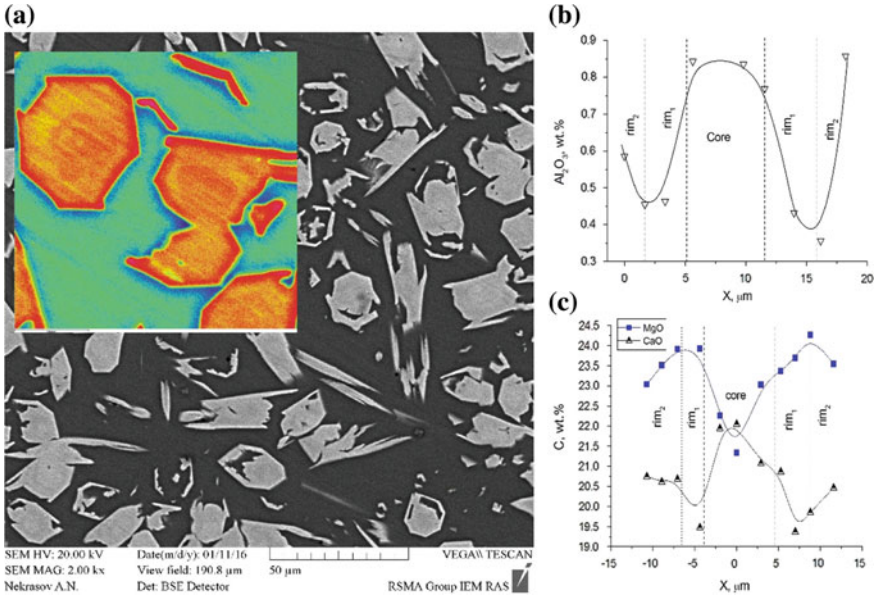


Fig. 5.5 Compositional zoning of clinopyroxene crystals from run 72. **a** BSE image of a Cpx crystal, on the inset an enlarged view of several crystals in false colors; three distinct zones can be seen, the outer quenching rim is morphologically unstable. **b** Profile of alumina concentration across a Cpx crystal; the core, the equilibrium and quenching rims can be distinguished. **c** Profiles of CaO and MgO concentrations across a Cpx crystal, there are the same zones as in the plot (**b**)

Detailed mapping of the composition of the largest crystals during the run 72 allowed us to more thoroughly check the correctness of our assumptions regarding the preservation of the CSD shape during quenching. The BSE images reflect the compositional zoning of the crystals and clearly demonstrate their cores. The CSD of these cores (surrounded by a zone with a low Al₂O₃ content), outlined manually on the BSE images, was acquired on the basis of the 70 counts. The procedure previously described (Eq. 2) and applied to the full CSD of run 72 led to an estimate of the quenching rim of the equilibrium crystals (dL) of 11 μm. The shift of the measured density function to a smaller size by 11 μm provided an estimate of the CSD at the equilibrium stage. The observed difference in the measured CSD of the cores with the transformed total CSD is not excessively large (see Fig. 5.6) in view of the low accuracy of the cores measurement data.

5.9 Discussion

It was found long ago that the thermal history of the melt in terms of the amount of the superheating above liquidus and its duration greatly affects the texture of the crystallization products (e.g., Donaldson 1979; Corrigan 1982). This effect took place

Table 5.4 The composition of experimental phases

Run #	Phase n/σ	SiO ₂	Al ₂ O ₃	MgO	CaO	Na ₂ O	K ₂ O	Total	Ab in glass (wt%)
48	Glass	66.43	13.89	1.86	1.74	8.30	0.16	92.52	89.43
	(6)	1.45	1.52	2.63	2.39	0.93	0.03		
	Di	55.87	1.14	20.34	21.40	0.55	0.03	99.58	
	(4)	0.43	0.16	0.28	0.27	0.09	0.04		
52	Glass	62.97	11.34	7.09	7.33	5.86	0.08	94.67	61.83
	(3)	0.49	0.08	0.07	0.47	0.16	0.01		
	Di	55.74	1.45	20.73	20.42	0.57	0.01	98.92	
	(3)	0.54	0.57	1.36	0.84	0.04	0.03		
60	Glass	68.90	14.79	1.05	0.07	9.26		94.06	96.30
	(5)	0.67	0.24	0.21	0.16	0.25			
	Di core	56.61	0.21	21.51	22.72	0.00		101.06	
	(3)	0.48	0.37	0.85	0.67	0.00			
51	Di rim	57.25	0.69	21.18	22.05	0.00		101.17	54.11
	(3)	0.14	0.75	1.42	0.45	0.00			
	Glass	63.91	9.93	9.12	8.71	5.52	0.10	97.30	
	(5)	0.93	0.28	0.55	0.39	0.32	0.07		
86	Glass	66.87	14.08	2.40	1.76	8.99	0.22	94.32	88.26
	(3)	0.76	0.30	0.35	0.54	0.10	0.11		
	Di	55.69	2.03	19.30	21.11	1.01	0.06	99.19	
	(3)	0.28	0.49	0.60	1.62	0.25	0.07		
72	Glass	68.29	14.65	0.77	0.51	7.72		92.16	95.82

(continued)

Table 5.4 (continued)

Run #	Phase $n/l\sigma$	SiO ₂	Al ₂ O ₃	MgO	CaO	Na ₂ O	K ₂ O	Total	Ab in glass (wt%)
54	(3)	0.36	0.65	0.20	0.07	0.11			
	Di core	55.16	0.78	20.49	21.78	0.32		98.61	
	(5)	0.01	0.40	1.12	0.49	0.20			
	Di rim	54.74	0.76	22.13	20.58	0.31		98.62	
	(5)	1.20	0.07	0.16	0.20	0.06			
	Di core	55.15	1.06	19.70	21.43	0.46		97.80	
	Di rim 1	54.61	0.46	21.44	21.55	0.26		98.32	
	Di rim 2	55.58	0.71	22.24	20.44	0.35		99.32	
	Glass	68.74	14.77	1.22	0.75	8.44	0.14	94.18	93.97
	(5)	0.50	0.27	0.22	0.21	0.32	0.05		
50	Di core	55.05	0.63	22.01	20.76	0.34	0.01	98.99	
	(5)	0.36	0.13	0.21	0.65	0.08	0.02		
	Di rim	55.47	0.76	22.24	20.32	0.38	0.06	99.46	
	(2)	0.25	0.06	0.57	0.06	0.06	0.08		
	Glass	66.91	13.86	1.93	2.28	8.09	0.15	93.32	87.91
	(5)	0.65	0.31	0.44	0.93	0.16	0.06		
	Di*	61.83	5.56	16.60	15.07	2.18	0.06	101.39	
	(3)	0.43	0.52	0.18	0.23	0.15	0.11		
	Glass	68.84	14.96	1.37	0.87	9.29	0.18	95.67	93.52
	(5)	1.04	0.37	0.28	0.47	0.30	0.08		
49	Di	57.69	2.51	19.06	20.26	1.16	0.06	100.95	

(continued)

Table 5.4 (continued)

Run #	Phase n/σ	SiO ₂	Al ₂ O ₃	MgO	CaO	Na ₂ O	K ₂ O	Total	Ab in glass (wt%)
56	(5)	0.82	1.56	1.90	2.93	0.66	0.04		
	Di core	55.73	1.18	20.00	22.41	0.68		100.00	
	Di core	56.8	1.29	19.85	22.69	0.58		101.21	
	Di rim	56.86	1.74	20.08	20.47	0.85		100.00	
61	Glass	68.71	15.11	2.31	2.46	8.43	0.14	97.37	87.13
	(5)	0.73	0.29	0.19	0.35	0.16	0.04		
	Di	55.96	1.03	21.42	21.71	0.45	0.03	100.78	
	(5)	0.41	0.32	0.45	0.25	0.10	0.03		
	Glass	70.04	13.48	1.80	0.78	8.05	0.12	94.31	91.52
	(4)	0.33	0.96	0.96	0.27	0.40	0.05		
61	Di core	55.98	0.69	21.12	22.25	0.34	0.02	100.41	
	(5)	0.28	0.28	0.39	0.35	0.17	0.03		
	Di rim	56.44	0.87	22.12	20.94	0.48	0.06	100.91	
	(6)	0.71	0.57	1.24	0.70	0.33	0.05		

The number of averaged analyses is in the parentheses under the phase name; line with single standard deviations is under the line with the corresponding oxide content. Di* corresponds to the mineral composition with some glass contribution due to the tiny crystal size, empty cells in K₂O column correspond to contents b.d.l.

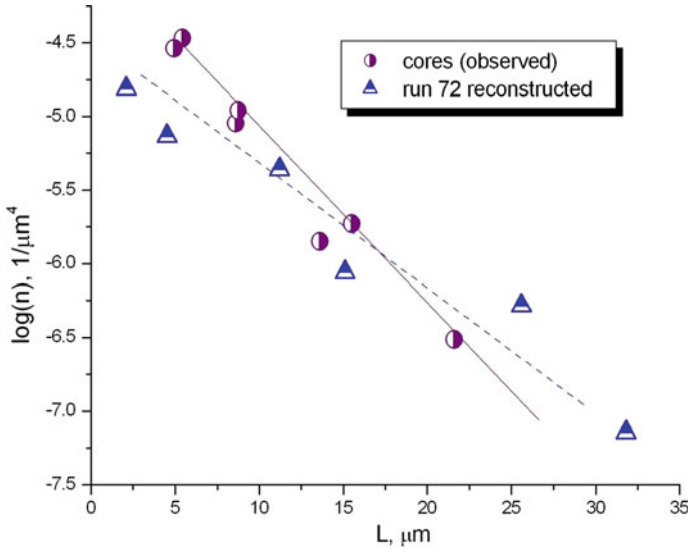


Fig. 5.6 The size distributions of the largest Cpx crystals from run 72; semi-filled stars depict the estimated CSD formed before quenching ($\epsilon_s = 0.046$), semi-filled circles display the CSD of the cores of large crystals approximately identified on the BSE images ($\epsilon_s = 0.036$). A fairly good agreement between the observed and theoretically reconstructed CSDs can be seen

in our experiments in which the melt overheated during the half-period of oscillations. The crystals were dissolved and the melt overheated with a sufficiently large period of oscillation. The speed and time of dissolution of the crystal is controlled by the diffusion rate of the slowest component, which is usually SiO_2 , unless cations with a high ionic potential are involved, such as Zr^{4+} or P^{5+} (Zhang et al. 2010).

Modeling dissolution of a crystal assemblage with a variable size stochastically distributed in space is a complex problem. The attribution of a certain volume of melt to each crystal (Bindeman and Melnik 2016) cannot be a realistic approximation in our case, because the number density sharply decreases in the experiments with a period of oscillation approaching the dissolution time. The number density of the residual crystals decreased during the hot half-cycle 25–30 times, which corresponds to an increase in the intercrystalline distance from 17 to 50 μm .

The simplest solution for dissolution time (t_{dissol}) of a spherical crystal in a diluted suspension, which is commonly used for scaling estimates, is as follows:

$$t_{dissol} = \frac{\rho_s \Delta C^* (1 - C_b) R_0^2 D_{\text{SiO}_2}}{2\rho_l}, \tag{4}$$

here ΔC^* is the difference between the solubility of Di at a given $T = 1155^\circ\text{C}$ (C_b) and initial content of the diopside in the melt during the equilibrium stage at $T = 1135^\circ\text{C}$ (C_{eq}) is corrected tentatively by a factor of 1/2 to account for the decreasing of the melt undersaturation over time. The smallest silica diffusivity D_{SiO_2} controls

the dissolution rate, and unequal crystal (ρ_s) and melt (ρ_l) densities are taken into account. The main uncertainty in the dissolution time is introduced by an estimate of the diffusion coefficient. As the first proxy we used the empirical model proposed in Mungal (2002), based on the composition of the melt and its viscosity calculated in accordance with Hui and Zhang (2007), and the diffusion coefficient of silica was evaluated by the value $D_{\text{SiO}_2} = 0.68 \times 10^{-8} \text{ cm}^2/\text{s}$. The concentration difference was read from the melting diagram (Fig. 5.1) $\Delta C = 0.042$. The dissolution time according to Eq. 4 is estimated to be 15–20 min at the maximal radius of the crystals $R_0 = 8\text{--}9 \text{ }\mu\text{m}$, respectively. A more accurate semi-analytical integration of the equation for the dissolution of a spherical crystal provides an approximately twice as long dissolution time of 30–40 min for the same R_0 range. This difference arises from the effective concentration difference on the surface of a dissolving crystal of actually less than one-half of the ΔC , when the effects of decreasing the volume of the melt and the composition of the melt approaching C_0 with time are included. Thus, the theoretical estimate of 30–40 min corresponds to the threshold value between incomplete and complete dissolution of crystals in the hot stage (groups three with half-period 20 min and four with half period 45–60 min).

Our experiments show that the almost complete dissolution of the crystals during the hot cycle gives the best result in terms of the rate of maturation (Fig. 5.7). During short times, both Mills and Glazner (2013) and Cabane et al. (2005) reported the average volume number content of crystals (N_v —zero-moment of CSD), which decrease with a rate proportional to approximately $t^{-1/5}$. In our experiments with an almost complete dissolution (group four), the volume content drops from $6.7\text{e-}03 \text{ }\mu\text{m}^{-3}$ (initial N_v) to $0.49\text{e-}03 \text{ }\mu\text{m}^{-3}$ in only two full cycles (run60) and to $2.04\text{e-}03 \text{ }\mu\text{m}^{-3}$ for four full cycles (run54). In these series, the CSDs shapes are nearly log-linear, with the slope rotating as the number of oscillations increases. In our experiments, the rate of nucleation in the cold half-period determines the number density and average crystal size. In general, the nucleation process in silicate melts is non-stationary (e.g., Tsuchiyama 1983) with a certain lag time in which stochastic processes take place in atomic-scale microclusters, with reaching a critical size and the formation of equilibrium microcrystals. Superheating greatly influences the distribution of clusters, so that with a sufficiently high or prolonged (or both) superheating, the delay time of nucleation increases and the rate of nucleation decreases. Davis and Ihinger (2002) are to our knowledge the only researchers that quantitatively modeled the impact of the size distribution of subcritical clusters on the kinetics of magma crystallization. Using their approach, it is possible to model the effect of superheating in the oscillating temperature regime on the nucleation rate and resultant CSD and quantitatively interpret our data.

Our experimental data justify an approximation of the growth rate independent of the crystal size, at a sufficiently small distance between the crystals. Whether crystal growth is controlled by diffusion or kinetics is important not only in the reconstruction the pre-quenching CSD (in the experiment, for minerals from volcanic rocks), but also for the evolution of CSD with repeated dissolution-precipitation events. This evolution can be modelled with a PDE solution for the distribution function (Simakin and Bindeman 2008). Van Westen and Groot (2018) used a simpler

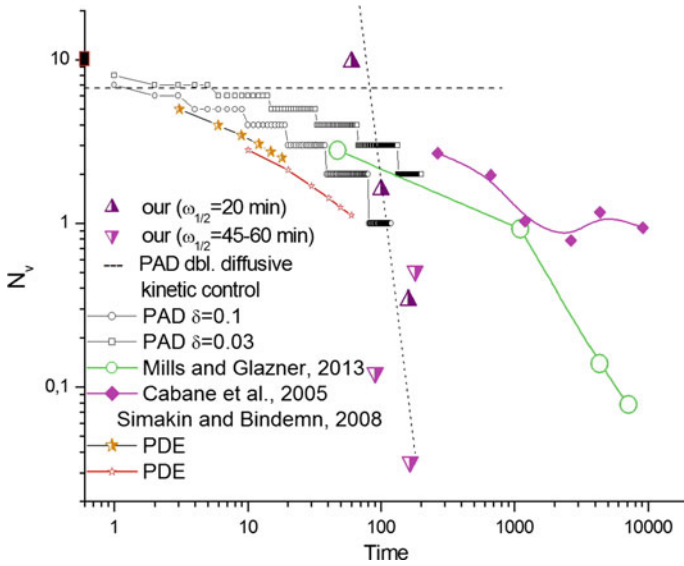


Fig. 5.7 Dependences of the volume crystal number content versus time during maturation in a crystal-melt mixture, as determined in various experimental studies and calculated with different methods. Our experimental data are shown with triangles, $N_v/4$ in μm^{-3} is plotted, time for all experiments in minutes. Results of the modeling with Particles Assemblage Dynamics (PAD) method (van Westen and Groot 2018) with open squares, squares and dashed line, δ is a volume fraction of crystals dissolved; N_v is total number of crystals, time is number of cycles; stars depict results of PDE solution for CSD from (Simakin and Bindeman 2008). In bi-logarithmic coordinates dimensionalities of N_v and time are inessential since slopes are invariants of scaling

method, manipulating a set of a finite number of crystals. The diffusion control is approximated by the square root dependence of each individual radius on time, which leads to the equation for the radii of the crystals R_i (crystals are ranked in order of increasing size) at the dissolution stage:

$$\sum_{i=n_1}^N (\sqrt{R_{i,k}^2 - \lambda_{1,k}})^3 = v_0(1 - \delta), \tag{5}$$

where δ is the volume fraction of dissolved crystals, n_1 is the number of the first crystal that survived the dissolution, and λ_1 is an unknown constant. For simplicity, we consider a small number of crystals $N = 10$; the crystals have an initial size $R_i = a i^2$ ($i = 1 \dots N$). The minimum number (n_1) satisfying Eq. (5) should be found numerically in each cycle. After finding λ_1^k new radii of the survived crystals with number $\geq n_1$ are calculated

$$R_{i,k+1/2} = \sqrt{R_{i,k}^2 - \lambda_{1,k}}, \quad i = n_1 \dots N \tag{6}$$

For a constant (independent of size) growth rate, the assumption of complete precipitation of the dissolved material in a cold half cycle requires:

$$\sum_{i=n1}^N (R_{i,k+1/2} + \lambda_{2,k})^3 = v_0, \quad (7)$$

With diffusion growth control, we obtain another equation similar to Eq. (5):

$$\sum_{i=n1}^N (\sqrt{R_{i,k+1/2}^2 + \lambda_{3,k}})^3 = v_0, \quad (8)$$

Final crystals sizes after $k + 1$ cycle of temperature oscillations are:

$$\begin{aligned} R_{i,k+1} &= R_{i,k+1/2} + \lambda_{2,k} \text{ and} \\ R_{i,k+1} &= \sqrt{R_{i,k+1/2}^2 + \lambda_{3,k}}, \quad i = n1..N, \end{aligned} \quad (9)$$

respectively. Numerical solution of the systems of Eqs. (5, 6) and (5, 7) gives completely different results. With kinetic control, the number of crystals reduces with time only to one. The calculated dependence $N(t) \approx at^{1/5}$ over a short time (number of steps) demonstrated a close resemblance to the experimental data of Cabane et al. (2005) and Mills and Glazner (2013) (see Fig. 5.7). Moreover, the theoretically obtained increase in the logarithmic slope of $N(t)$ at the larger time was observed by Mills and Glazner (2013). The Ostwald ripening corresponds to a larger logarithmic slope $n = at^{1/3}$ (Lifshitz and Slyozov 1961). Reducing the degree of dissolution [setting a smaller δ value in Eq. (5)] leads to the slower ripening with a close initial logarithmic slope just as shown in Cabane et al. (2005), where small stochastic temperature oscillations were caused by temperature regulation. When both dissolution and growth are controlled by diffusion, only the first cycle in our calculations reduces the number of crystals without changing the number and size of crystals in subsequent cycles. With double diffusion control, similar results are obtained when using a larger number of crystals for modeling, which allows to calculate the density function of CSD (Van Westen and Groot 2018). In the first cycles, the distribution was changed, and then modified only by Ostwald ripening, due to the size dependence of the solubility of the crystals, whereas the temperature cycle did not affect the shape of the CSD.

5.10 Conclusions

The crystallization of clinopyroxene from a melt in the Ab-Di-H₂O system at $P = 200$ MPa with temperature oscillations around the liquidus was investigated. A procedure is proposed for the recovery of CSD of clinopyroxene at the stage before

quenching, which correctly removes the quenching portion of the distribution. This procedure is based on the assumption that the growth rate does not depend on the crystal size. The recovery of CSD was successfully validated for the run with sufficiently large Cpx crystals, for which cores formed at the main stage of the experiment can be distinguished in the BSE images. Our experiments showed that the texture of crystallization products, characterized by CSD, strongly depends on the period of temperature oscillations. The maximum temperature during the oscillations was above the liquidus of diopside, which completely dissolved when the duration of the hot half period was above 30–40 min. Then the nucleation and growth of diopside in each cold half-period results in a log-linear CSD. With a period of oscillation of 4–10 min, Cpx crystals were only partially dissolved in the melt at the hot stage and re-precipitated at the cold one. In this case, CSD of clinopyroxene gradually developed to a log-normal like shape, as in previous studies. By simple calculations, it was demonstrated that the crystal number density decreases and mean radius increases only when the crystals grow in a kinetic (size independent) mode and dissolve at the diffusion control.

Acknowledgements Study was done within theme AAAA-A18-118020590141-4 of the State task of IEM RAS for 2019–2021.

References

- Avrami M (1939) Kinetics of phase change. I. General theory. *J Chem Phys* 7(12):1103–1112
- Bindeman IN, Melnik OE (2016) Zircon Survival, Rebirth and recycling during crustal melting, magma crystallization, and mixing based on numerical modelling. *J Petrol* 57(3):437–460
- Boyd FR, Schairer JF (1964) The system $MgSiO_3$ - $CaMgSi_2O_6$. *J Petrol* 5:275–309
- Brandeis G, Jaupart C, Allegre CJ (1984) Nucleation, crystal growth, and the thermal regime of cooling magmas. *J Geophys Res* 89:10161–10177
- Cabane H, Laporte D, Provost A (2005) An experimental study of Ostwald ripening of olivine and plagioclase in silicate melts: implications for the growth and size of crystals in magmas. *Contrib Mineral Petr* 150(1):37–53. <https://doi.org/10.1007/s00410-005-0002-2>
- Cashman KV, Marsh BD (1988) Crystal size distribution (CSD) in rocks and the kinetics and dynamics of crystallization, II, Makaopuhi lava lake. *Contrib Mineral Petr* 99:292–305
- Chekhmir AS, Simakin AG, Epel'baum MB (1991) Dynamic phenomena in fluid-magma systems. Nauka, Moscow, 141 p. (in Russian)
- Corrigan GM (1982) Supercooling and the crystallization of plagioclase, olivine, and clinopyroxene from basaltic magmas. *Mineral Mag* 46:31–42
- Davis MJ, Ihinger PD (2002) Effects of thermal history on crystal nucleation in silicate melt: numerical simulations. *J Geophys Res* 107(B11):2284. <https://doi.org/10.1029/2001jb000392>
- Donaldson CH (1979) An experimental investigation of the delay in nucleation of Olivine in Mafic magmas. *Contrib Mineral Petr* 69:21–32
- Epel'baum MB (1980) Silicate melts with volatile components. Nauka, Moscow, 255 p. (in Russian)
- Higgins MD (2000) Measurement of crystal size distributions. *Am Mineral* 85:1105–1116
- Higgins MD (2002) A crystal size-distribution study of the Kiglapait layered mafic intrusion, Labrador, Canada: evidence for textural coarsening. *Contrib Mineral Petr* 144:314–330

- Hort M (1998) Abrupt change in magma liquidus temperature because of volatile loss or magma mixing: effects on nucleation, crystal growth and thermal history of the magma. *J Petrol* 39(5):1063–1076
- Hui H, Zhang Y (2007) Toward a general viscosity equation for natural anhydrous and hydrous silicate melts. *Geochim Cosmochim Acta* 71:403–416
- Lifshitz IM, Slyozov VV (1961) The kinetics of precipitation from supersaturated solid solution. *J Phys Chem Solids* 19:35–50
- Marsh BD (1988) Crystal size distribution (CSD) in rocks and the kinetics and dynamics of crystallization. I Theory *Contrib Mineral Petr* 99(3):277–291
- McMillan PF, Holloway JR (1987) Water solubility in aluminosilicate melts. *Contrib Mineral Petr* 97:320–332
- Mills RD, Glazner AF (2013) Experimental study on the effects of temperature cycling on coarsening of plagioclase and olivine in an alkali basalt. *Contrib Mineral Petr* 166:97–111
- Mungall JE (2002) Empirical models relating viscosity and tracer diffusion in magmatic silicate melts. *Geochim Cosmochim Acta* 66(1):125–143
- Ni H, Keppler H, Walte N, Schiavi F, Chen Y et al (2014) In situ observation of crystal growth in a basalt melt and the development of crystal size distribution in igneous rocks. *Contrib Mineral Petr* 167:1003
- Pati JK, Arima M, Gupta AK (2000) Experimental study of the system diopside-albite-nepheline at $P(\text{H}_2\text{O}) = P(\text{total}) = 2$ and 10 kbar and at $P(\text{total}) = 28$ kbar. *Can Mineral* 38:1177–1191
- Simakin AG, Bindeman IN (2008) Evolution of crystal sizes in the series of dissolution and precipitation events in open magma systems. *J Volcanol Geoth Res* 177:997–1010
- Simakin AG, Chevychelov VY (1995) Experimental studies of feldspar crystallization from the granitic melt with various water content. *Geochem Intl* 38:523–534
- Simakin AG, Salova TP (2004) Plagioclase crystallization from a hawaiitic melt in experiments and in a volcanic conduit. *Petrology* 12(1):82–92
- Simakin AG, Trubitsyn VP, Kharybin EV (1998) The size and depth distribution of crystals settling in a solidifying magma chamber. *Izv-Phys Solid Eart* 34(8):639–646
- Simakin A, Armienti P, Epel'baum M (1999) Coupled degassing and crystallization: experimental study at continuous pressure drop, with application to volcanic bombs. *Bull Volcanol* 61:275. <https://doi.org/10.1007/s004450050297>
- Simakin AG, Salova TP, Armienti P (2003) Kinetics of clinopyroxene growth from a hydrous hawaiite melt. *Geochem Int* 41(12):1165–1175
- Toramaru A (1991) Model of nucleation and growth of crystals in cooling magmas. *Contrib Mineral and Petrol* 108:106. <https://doi.org/10.1007/bf00307330>
- Tsuchiyama A (1983) Crystallization kinetics in the system $\text{CaMgSi}_2\text{O}_6$ - $\text{CaAl}_2\text{Si}_2\text{O}_8$: the delay in nucleation of diopside and anorthite. *Am Mineral* 68:687–698
- Van Westen T, Groot RD (2018) Effect of temperature cycling on ostwald ripening. *Cryst Growth Des* 18(9):4952–4962. <https://doi.org/10.1021/acs.cgd.8b00267>
- Vona A, Romano C (2013) The effects of undercooling and deformation rates on the crystallization kinetics of Stromboli and Etna basalts. *Contrib Mineral Petr* 166(2):491–509
- Vona A, Romano C, Dingwell DB, Giordano D (2011) The rheology of crystal-bearing basaltic magmas from Stromboli and Etna. *Geochim Cosmochim Acta* 75:3214–3236
- Yoder HS (1965–1966) Carnegie Institution, Washington, Year book, 65 274 1966. Carnegie Institution of Washington, Washington DC
- Zhang Y, Ni H, Chen Y (2010) Diffusion data in silicate melts. *Rev Mineral Geochem* 72:311–408